Special Issue – TANGO

International journal of spray and combustion dynamics

International Journal of Spray and Combustion Dynamics
0(0) 1–13

DOI: 10.1177/1756827717728056
journals.sagepub.com/home/scd

SAGE

Nonlinear analytical flame models with amplitude-dependent time-lag distributions

Sreenath M Gopinathan[1], Dmytro Iurashev[2], Alessandra Bigongiari[1] and Maria Heckl[1]

Abstract

In the present work, we formulate a new method to represent a given Flame Describing Function by analytical expressions. The underlying idea is motivated by the observation that different types of perturbations in a burner travel with different speeds and that the arrival of a perturbation at the flame is spread out over time. We develop an analytical model for the Flame Describing Function, which consists of a superposition of several Gaussians, each characterised by three amplitude-dependent quantities: central time-lag, peak value and standard deviation. These quantities are treated as fitting parameters, and they are deduced from the original Flame Describing Function by using error minimisation and nonlinear optimisation techniques. The amplitude-dependence of the fitting parameters is also represented analytically (by linear or quadratic functions). We test our method by using it to make stability predictions for a burner with well-documented stability behaviour (Noiray's matrix burner). This is done in the time-domain with a tailored Green's function approach.

Keywords

Flame transfer function, amplitude-dependence, multiple time-lags, Green's function, stability analysis

Date received: 31 May 2017; accepted: 30 July 2017

1. Introduction

Power generation systems based on combustion of fuels to extract energy operate with lean premixed flames in order to reduce the pollution of the environment by exhaust gases. However, such systems are susceptible to thermoacoustic instabilities, which are characterised by high-amplitude acoustic oscillations caused by the feedback between oscillations in pressure and heat release rate. These oscillations lead to excessive vibration of structural components and, in extreme cases, major hardware damage.[1]

The relationship between the heat release rate and the acoustic field is a crucial element in modelling thermoacoustic instabilities. This relationship may be given in the time-domain or frequency-domain. For example, the commonly used $n\tau$-law[2] reads

$$\frac{Q'(t)}{\bar{Q}} = n\frac{u'(t-\tau)}{\bar{u}}. \tag{1}$$

in the time-domain, and

$$\frac{\hat{Q}(\omega)}{\bar{Q}} = ne^{i\omega\tau}\frac{\hat{u}(\omega)}{\bar{u}}. \tag{2}$$

in the frequency-domain, where n is the coupling coefficient and τ is the time-lag. We use the following notation: $e^{-i\omega t}$ for the time dependence, $Q'(t)$ for the fluctuation of the heat release rate in the time-domain, $\hat{Q}(\omega)$ for its frequency-domain equivalent (Fourier transform), and $\bar{Q}$ for the mean rate of heat release; the same notation is used for the acoustic velocity, u (at a chosen reference position upstream of the

[1]School of Chemical and Physical Sciences, Keele University, Staffordshire, UK
[2]DICCA, Università degli Studi di Genova, Genoa, Italy

Corresponding author:
Maria Heckl, School of Chemical and Physical Sciences, Keele University, Staffordshire ST55BG, UK.
Email: m.a.heckl@keele.ac.uk

flame). In general, the time-domain expression is given in terms of a functional F,

$$\frac{Q'(t)}{\bar{Q}} = F\left[\frac{u'(t)}{\bar{u}}\right]. \quad (3)$$

and the frequency-domain expression by the flame transfer function (FTF) denoted by $\mathcal{T}(\omega)$,

$$\mathcal{T}(\omega) = \frac{\hat{Q}(\omega)/\bar{Q}}{\hat{u}(\omega)/\bar{u}}. \quad (4)$$

The FTF may depend on the amplitude of the velocity, in which case it is referred to as 'flame describing function' (FDF).

The FTF or FDF of a given burner can be measured, and the result is a sequence of complex numbers at discrete frequencies. For analytical modelling purposes, it is necessary to convert such data into a continuous function of frequency. This is typically done by some ad hoc curve-fitting procedure. Several examples can be found in the literature: Schuermans[3] and Schuermans et al.[4] measured the FTF of a turbulent partially premixed burner and approximated it by a superposition of two Gaussian curves. Komarek and Polifke[5] measured the FTF of a perfectly premixed swirl burner (the 'BRS burner') and approximated it with three Gaussians. Each Gaussian was centred around a specific delay time, which corresponded to the travel of a specific perturbation quantity, such as swirl number. A similar approach was used by Bade et al.:[6] they approximated the FTF measured for an annular combustor by a superposition of a low-pass filtered discrete time-lag term and two distributed time-lag terms. Subramanian et al.[7] approximated the FTF of the BRS burner by using a superposition of rational functions with fitting parameters. Noiray[8] and Noiray et al.[9] considered also the amplitude-dependence; they measured the FDF of a matrix burner and approximated it with a straightforward interpolation. Ćosić et al.[10] measured the FDF of a partially premixed swirl burner and approximated it in a similar way.

The FTF or FDF of a given burner can also be determined by numerical simulations. Some flame models are based on the idea that the time it takes a fuel particle to travel from the nozzle to the point of combustion differs slightly from particle to particle, and this can be described in terms of a histogram or distribution. Polifke et al.[11] simulated a burner with an elliptical premix nozzle by steady-state CFD and used Lagrangian particle tracking to determine a histogram of arrival times. This turned out to be similar to a Gaussian curve and was approximated accordingly. Flohr et al.[12,13] performed a similar simulation for a dump combustor; they found a distribution of time-lags, which was reminiscent of a superposition of two Gaussian distributions, centred around two peak values. Similar simulations were performed by Schuermans[3] and Schuermans et al.[4] for their premixed swirl burner; again, two Gaussian distributions were obtained. These were found to be associated with the travel times of two different physical phenomena: fluctuations in turbulence intensity and fluctuations in fuel concentration.

More recently, flame models have been obtained with accurate, but computationally demanding, unsteady CFD simulations. These generate the time histories for heat release rate and velocity; by application of the Wiener–Hopf inversion, the FTF is then determined. An example is the work by Tay-Wo-Chong et al.[14] who calculated the FTF of the BRS burner in this way (using LES). This work was extended into the nonlinear domain by Iurashev et al.,[15] who performed simulations with four different forcing amplitudes.

Stability predictions for a particular combustion system can be made by combining a model for the unsteady acoustic field in the combustor with a model for its FTF. If additional amplitude information is available in the form of an FDF, predictions can also be obtained for limit cycle amplitudes. Linear stability predictions were made, for example, by Heckl[16] and Tay-Wo-Chong et al.;[14] Tay-Wo-Chong et al.[14] found that small errors in the FTF can make such predictions quite inaccurate.

Nonlinear stability predictions were obtained by some of the authors quoted above: Noiray; Noiray[8]; Noiray et al.[9] treated the length L of the plenum chamber as a continuously variable control parameter and produced a 'stability map' in the L–A plane (A is the amplitude of the velocity perturbation). These maps gave not only the linear stability behaviour, but also revealed limit cycle amplitudes and hysteresis behaviour. Palies et al.[17] studied a premixed swirl combustor with the length of the combustion chamber as control parameter and obtained similar stability maps. Ćosić et al.[10] predicted limit cycle amplitudes for their burner, and these were in good agreement with experimental results.

Li and Morgans[18] made nonlinear stability predictions for a horizontal Rijke tube. They modelled the heat source analytically by an extended $n\tau$-law with the following features: single time-lag; no time-lag distribution; saturation amplitude imposed on the heat release rate; cut-off frequency imposed on the FTF to capture its low-pass filter behaviour. They used a wave based approach to model the acoustic field.

The current paper builds on the work by Heckl,[16,19] who developed a simple time-lag law for Noiray's matrix flame.[8,9] This law included a time-delayed velocity term, $u(t-\tau)$, and an instantaneous velocity term, $u(t)$, each with its own coupling coefficient, but zero

standard deviation. The amplitude-dependence was in the time-lag and in the coupling coefficients, and it was represented by simple functions. This model captured some relevant features of the FTF (excess gain, near-constant phase), but not the low-pass behaviour. Nevertheless, the model gave good stability predictions (using a tailored Green's function approach), which were in line with Noiray's stability map. Bigongiari and Heckl[20] also used the same heat release rate law for a Rijke tube and obtained its stability behaviour using tailored Green's function.

The aim of our paper is to introduce a generic FDF in analytical form, representing both the frequency-dependence *and* the amplitude-dependence analytically. The underlying idea is that the unit impulse response (UIR), which is effectively a time-lag histogram, is a superposition of distributions, each characterised by a mean time-lag, standard deviation and peak value. This idea is motivated by the following observations:

(i) Different types of perturbations (e.g. perturbation of swirl number, perturbation of fuel concentration, vortices, perturbation of turbulence intensity) travel with different speeds.
(ii) The arrival of a perturbation at the flame is spread out over time.

We assume the individual distributions to be Gaussian, with central time-lags $\tau_1, \tau_2, \ldots$ and standard deviations $\sigma_1, \sigma_2, \ldots$; they are also described by generalised coupling coefficients $n_1, n_2, \ldots$. These quantities will be treated as fitting parameters, which are amplitude-dependent and chosen to fit a given FDF; their amplitude-dependence will be described by simple functions (linear or quadratic).

Our representation of the FDF is very general and can be adapted to model any of the flames mentioned in the literature survey above. We expect that it can be applied to many more flames, given that the rationale behind it is motivated by the transport phenomena typically observed in combustion systems. Since its basic idea is rooted in the time-domain, our method also provides the time-domain representation of the heat release law in analytical form. This is very useful for performing time-domain simulations with a minimum of numerical effort.

The mathematical formulation of our method is explained in section 2, followed by a case study in section 3. We use Noiray's matrix burner[8,9] as the case study example. The matrix burner and its measured FDF are described in section 3.1. The UIR of the matrix flame is given in section 3.2, and is converted into an analytical FDF in section 3.3. The tailored Green's function for the matrix burner can be calculated analytically, and the results are given in section 3.4. It forms the basis of the stability analysis, which is given in section 3.5. Stability predictions are made and discussed in section 3.6. The paper concludes with a summary and suggestions for further work in section 4.

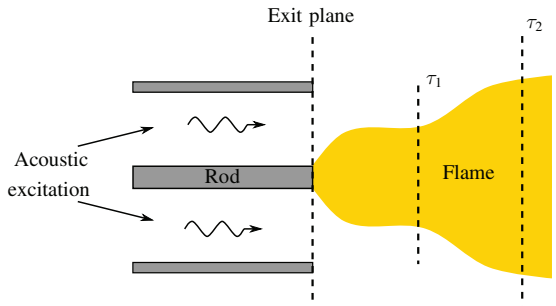

Figure 1. Schematic of a flame showing distribution of time-lags.

2. Gaussian time-lag distributions

We consider the burner set-up shown in Figure 1. A flame of finite extent is located downstream of a nozzle; the exit plane of the nozzle is taken as reference position. Flow perturbations leaving the exit plane reach the flame front at different time instances and therefore there is a distribution of time-lags causing delayed heat release rate fluctuations. This suggests the following generalised law for the heat release rate in the time domain

$$\frac{Q'(t)}{\bar{Q}} = \int_0^\infty h(\tau)\frac{u'(t-\tau)}{\bar{u}}\mathrm{d}\tau. \tag{5}$$

h is a generalised coupling coefficient and depends on the time-lag τ. Moreover, it is identical with the UIR of the flame, as has been shown in Gopinathan et al.[21]

The dynamic behaviour of many flames is characterised by two or more prominent time-lags, and by a distribution of the heat release rate around these time-lags. Let us assume a generic heat release rate law with k prominent time-lags $\tau_1, \tau_2, \ldots, \tau_k$, and with a Gaussian distribution D centred around each of them,

$$\begin{aligned}\frac{Q'(t)}{\bar{Q}} = {} & n_1\int_0^\infty \frac{u'(t-\tau)}{\bar{u}}D(\tau-\tau_1)\mathrm{d}\tau \\ & + n_2\int_0^\infty \frac{u'(t-\tau)}{\bar{u}}D(\tau-\tau_2)\mathrm{d}\tau + \cdots \\ & + n_k\int_0^\infty \frac{u'(t-\tau)}{\bar{u}}D(\tau-\tau_k)\mathrm{d}\tau,\end{aligned} \tag{6}$$

where D is given by

$$D(\tau-\tau_j)=\frac{1}{\sigma_j\sqrt{2\pi}}e^{(-(\tau-\tau_j)^2/2\sigma_j^2)},\qquad j=1,2,\ldots,k \quad (7)$$

Equation (6) contains $3k$ parameters, τ_1, τ_2,..., τ_k, n_1, n_2,..., n_k, and σ_1, σ_2,..., σ_k, which are treated as fitting parameters and assumed to be amplitude-dependent. We presume that the distributions are close to zero for negative τ; then we can extend the integration range in equation (6) from $(0, \infty)$ to $(-\infty, +\infty)$ and apply the Fourier transform. This leads to the FDF (for details, see Appendix 1).

$$\begin{aligned}\mathcal{T}_k(\omega,A)&=\frac{\hat{Q}(\omega,A)/\bar{Q}}{\hat{u}(\omega,A)/\bar{u}}\\&=n_1(A)e^{-\omega^2\sigma_1(A)^2/2}e^{i\omega\tau_1(A)}\\&\quad+n_2(A)e^{-\omega^2\sigma_2(A)^2/2}e^{i\omega\tau_2(A)}+\cdots\\&\quad+n_k(A)e^{-\omega^2\sigma_k(A)^2/2}e^{i\omega\tau_k(A)}.\end{aligned} \quad (8)$$

The unknown fitting parameters in this representation are determined by minimising the difference between the original FDF, $\mathcal{T}(\omega, A)$, and the expression for $\mathcal{T}_k(\omega, A)$ given in equation (8). We do this by using the optimisation routine `lsqnonlin` in MATLAB®, with the error defined by the vector

$$\epsilon_k=\left\{\sqrt{|\Re[\mathcal{T}(\omega,A)-\mathcal{T}_k(\omega,A)]|},\ \sqrt{|\Im[\mathcal{T}(\omega,A)-\mathcal{T}_k(\omega,A)]|}\right\}. \quad (9)$$

The vector ϵ_k contains the real part and imaginary part of the difference; it has $2N$ components, where N is the number of data points along the ω-axis. We also impose the additional constraint that $|\mathcal{T}_k(\omega, A)| = 1$ at $\omega = 0$, which gives

$$\sum_{j=1}^{k}n_j=1. \quad (10)$$

The error minimisation procedure is repeated for each amplitude A for which data are available. The analytical representation of any known FDF can be obtained using this procedure if the complex values of the FDF are known for a sufficient number of frequency points at specific amplitudes.

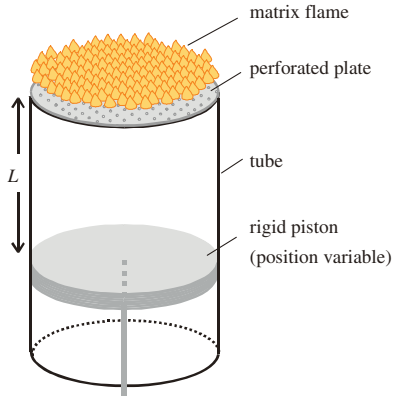

Figure 2. Schematic of Noiray's matrix burner.

3. Case study: Noiray's matrix burner

3.1 Description of the matrix burner

The matrix burner used in Noiray's work (Figure 2) consists of a circular tube with a piston (variable position) at one end and a perforated plate at the other end. The perforated plate acts as the flame holder for a 2D array (matrix) of small flames. The tube is essentially a quarter-wave resonator, with one rigid end and one nearly open end. The acoustic field in the tube extends slightly beyond the downstream end and reaches the flames, making thermoacoustic interaction possible.

Noiray et al.[9] measured the FDF by exciting a harmonic sound field in the tube with a loudspeaker. The excitation frequencies were in the range [0, 1200 Hz], and 5 excitation amplitudes were used: $A/\bar{u} = 0.13$, 0.23, 0.40, 0.48, 0.54. The velocity fluctuations were measured by Laser Doppler Velocimetry at the base of the flame (i.e. the reference position for their FDF was the same as the flame position). The ensuing fluctuations of the rate of heat released by the matrix flame (global heat release) were measured by chemiluminescence, using a photomultiplier tube equipped with OH* filter. The measured results are shown by the markers in Figure 3 for the gain ($|FTF|$, left) and the phase ($\angle FTF$, right).

The gain ($|FTF|$) shows a low pass filter behaviour and reaches values in excess of 1 at low frequencies. The maximum value decreases with increasing excitation amplitude, and the position of the maximum shifts to lower frequencies. The phase ($\angle FTF$) curve is approximately linear at low frequencies, with a slope that increases with increasing excitation amplitude.

3.2 UIR of the matrix flame

In a first step towards obtaining an analytical expression for the measured results in Figure 3, we determine

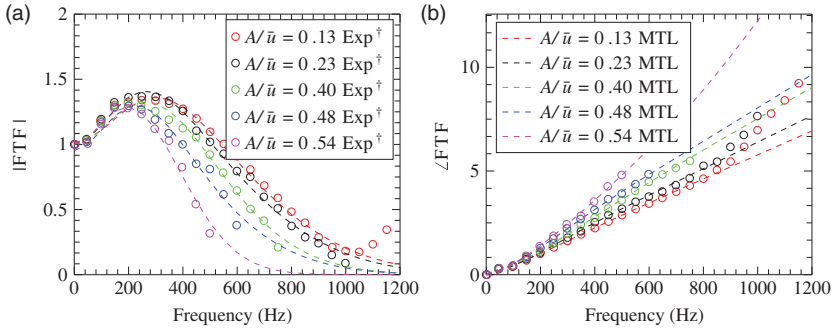

Figure 3. Gain (left) and phase (right) vs frequency for the FDF of Noiray's matrix flame. Markers: experimental values from Noiray et al.[9] Dashed curves: analytical approximation based on equation (12) using the expressions given in Table 1.
FDF: Flame Describing Function.

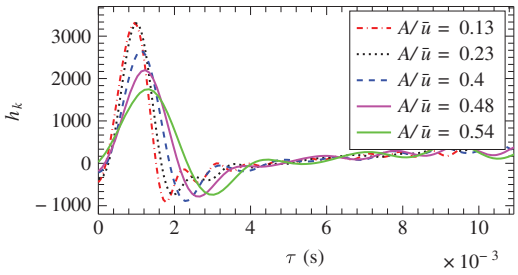

Figure 4. Impulse response of the matrix flame.

the corresponding UIR. The UIR is the response of the flame (in terms of the heat release rate) triggered by a normalised velocity impulse. Its general definition is given by equation (5). For realistic flames (i.e. flames that satisfy causality), the UIR is zero for negative τ-values (causality) and again for τ-values beyond some maximum (finite duration of response). We take this maximum value to be equal to the slope of the phase curve at low frequencies and denote it by $\tau_\angle$. Then equation (5) becomes (after a substitution for the integration variable τ with $t-\tau$

$$\frac{Q'(t)}{\bar{Q}} = \int_0^{t_\angle} h(\tau)\frac{u'(t-\tau)}{\bar{u}}\,\mathrm{d}\tau. \qquad (11)$$

We calculated the UIR of the matrix burner flame by the inverse z-transform of the FTF as described in Polifke.[22] To calculate the inverse z-transform, the time interval $[0, \tau_\angle]$ is discretised into 150 equally spaced points (this number of points was chosen because it gives a smooth UIR vs time-lag curve). The results are shown in Figure 4 for the five amplitude values $A/\bar{u} = 0.13, 0.23, 0.40, 0.48, 0.54$. We observe that there are two prominent time-lags in the UIR for all values of $A/\bar{u}$. For example, at $A/\bar{u} = 0.13$, there is one near $\tau_1 = 0.001s$, where the UIR has a maximum, and one near $\tau_2 = 0.002s$, where the UIR has a (negative) minimum. There are some further maxima and minima at larger time-lags, but they are minor. We therefore conclude that the FDF can be approximated with a distribution around two central time-lags τ_1 and τ_2. As $A/\bar{u}$ increases, both τ_1 and τ_2 increase, the peak value of the maximum decreases, and the minimum value around τ_2 becomes less negative.

3.3 Analytical description of the matrix flame

We now proceed to represent the FDF shown in Figure 3 by the analytical expression in equation (8) with only two terms included in the expression for the FDF,

$$\mathcal{T}_2(\omega, A) = n_1(A)e^{-\omega^2\sigma_1(A)^2/2}e^{i\omega\tau_1(A)} + n_2(A)e^{-\omega^2\sigma_2(A)^2/2}e^{i\omega\tau_2(A)}. \qquad (12)$$

The unknown fitting parameters n_1, n_2, τ_1, τ_2, σ_1 and σ_2 are determined as described in section 2. This is done individually for each of the five available amplitude values $A/\bar{u} = 0.13, 0.23, 0.40, 0.48, 0.54$. The results are shown by the markers in Figure 5.

All fitting parameters vary with amplitude. n_1 and σ_2 seem to decrease with increasing amplitude, while n_2 and σ_1 seem to increase; all have considerable scatter. The results for τ_1 and τ_2 clearly increase with amplitude, and this increase appears to be faster than linear. We model this amplitude-dependence analytically by linear functions for n_1, n_2, σ_1 and σ_2, and by quadratic functions for τ_1 and τ_2. These functions are shown by the dashed curves in Figure 5 and are listed in Table 1. The coefficients in these functions were obtained by linear least squares estimation.

Altogether, the combination of equation (12) and the functions in Table 1 provides a fully analytical representation for the FDF in Figure 3. This also provides an extrapolation to frequency and amplitude values for which experimental data are not available. Plots of the

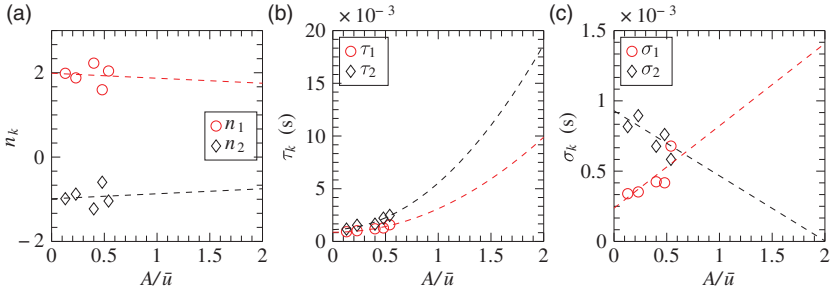

Figure 5. Amplitude-dependence of the fitting parameters n_1, n_2 (part (a)), τ_1, τ_2 (part (b)) and σ_1,σ_2 (part (c)). Markers: results for individual amplitudes. Dashed curves: approximation (and extrapolation) by the analytical functions in Table 1.

Table 1. Analytical approximation of the amplitude-dependence of the fitting parameters.

Parameter	Dependence on $A/\bar{u}$
n_1	$-1.185 \times 10^{-1}(A/\bar{u}) + 1.99$
n_2	$1.185 \times 10^{-1}(A/\bar{u}) - 0.99$
τ_1	$2.28 \times 10^{-3}(A/\bar{u})^2 - 4.74 \times 10^{-05}(A/\bar{u}) + 8.7 \times 10^{-4}$
τ_2	$4.35 \times 10^{-3}(A/\bar{u})^2 + 6.79 \times 10^{-05}(A/\bar{u}) + 1.12 \times 10^{-3}$
σ_1	$5.86 \times 10^{-4}(A/\bar{u}) + 2.36 \times 10^{-4}$
σ_2	$-4.63 \times 10^{-4}(A/\bar{u}) + 9.3 \times 10^{-4}$

analytical expressions (equation (12) and Table 1) have been added to Figure 3 in the form of dashed curves. A comparison with the experimental results (markers in Figure 3) shows that the analytical representation is very accurate.

Manipulating the expression for the $\mathcal{T}_2(\omega, A)$ in equation (12), we can write the gain and phase as (derivations not given in this paper),

$$|\mathcal{T}_2(\omega, A)| = \sqrt{n_1 e^{\frac{-\omega^2\sigma_1^2}{2}} + n_2 e^{\frac{-\omega^2\sigma_2^2}{2}} + 2n_1 n_2 e^{\frac{-\omega^2(\sigma_1^2+\sigma_2^2)}{2}} \cos\omega(\tau_2 - \tau_1)}, \quad (13)$$

$$\arg(\mathcal{T}_2(\omega, A)) = \frac{n_1 \sin\omega\tau_1 + e^{\frac{-\omega^2(\sigma_1^2-\sigma_2^2)}{2}} n_2 \sin\omega\tau_2}{n_1 \cos\omega\tau_1 + e^{\frac{-\omega^2(\sigma_1^2-\sigma_2^2)}{2}} n_2 \cos\omega\tau_2}, \quad (14)$$

Valuable interpretations can be obtained from these equations for the gain and phase of $\mathcal{T}_2(\omega, A)$. Equation (13) shows that the gain depends on the time-lag *difference* $\tau_1 - \tau_2$, but not on the time-lags individually. Of the three terms under the square-root, only the third term is oscillatory; $\cos\omega(\tau_2 - \tau_1)$ is periodic along the ω-axis and has a maximum at the frequency value $\omega_{\max} = 2\pi/(\tau_2 - \tau_1)$, and hence the gain attains a maximum there. Figure 3 shows that ω_{max} moves to lower ω-values as $A/\bar{u}$ increases, and we can therefore conclude that $\tau_2 - \tau_1$ must increase with increasing $A/\bar{u}$. This is also the case for the analytical representation, as can be seen in Figure 5(b). Equation (14) shows that the phase of the FTF depends on the *difference* $\sigma_1^2 - \sigma_2^2$, but not on σ_1 or σ_2 individually. If $\sin\omega\tau$ and $\cos\omega\tau$ in equation (14) are approximated to $\mathcal{O}(\omega)$, the phase becomes $\omega(n_1\tau_1 + n_2\tau_2)/(n_1 + n_2)$, i.e. the phase curve starts with a slope which is given by a 'weighted time-lag'.

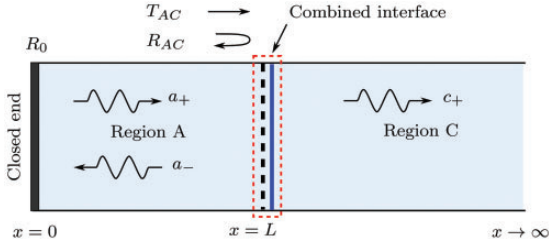

Figure 6. The modelled configuration, showing the acoustic waves and reflection and transmission coefficients.

3.4 Analytical model for the burner configuration in terms of its tailored Green's function

In order to model set-up in Figure 2 analytically, we make the following assumptions:

1. The sound field is purely 1D, not only inside the tube, but also beyond its downstream end. The wave transmitted beyond this end is of course 3D, but we ignore this and instead assume that the tube has a semi-infinite continuation, which keeps the transmitted wave 1D. There are forward and backward travelling acoustic waves inside the tube (shown in Figure 6 by a_+ and a_-) and just a forward travelling wave (shown by c_+) in the semi-infinite continuation section.
2. We model the downstream end as a combined interface (see Figure 6) consisting of a perforated plate at

$x = L$, and an open end at $x = L + \Delta$; each interface has a given reflection and transmission coefficient; the distance Δ between them is very small, $\Delta \to 0$.
3. The upstream end is modelled as rigid wall with a reflection coefficient of $R_0 = 1$.
4. The mean temperature and speed of sound (denoted by c) are uniform throughout the semi-infinite tube.

The pressure reflection and transmission coefficient for individual interfaces (perforated plate and open end) and the combined interface of the configuration in Figure 6 have been derived in Heckl.[16] R_{AC} and T_{AC} are the reflection and transmission coefficients at the combined interface for waves travelling in the forward direction and R_{CA} and T_{CA} are the reflection and transmission coefficients for waves travelling in the backward direction. The expressions for these reflection and transmission coefficients are given in Appendix 2. Interested readers are advised to refer to Heckl[16] for more details.

The Green's function $G(x, x', t - t')$ is the response observed at position x and time t to a point source at position x' firing an impulse at time t'. Its governing equation is

$$\frac{1}{c^2}\frac{\partial^2 G}{\partial t^2} - \frac{\partial^2 G}{\partial x^2} = \delta(x - x')\delta(t - t'). \tag{15}$$

The *tailored* Green's function[16,23] is the solution of equation (15), which satisfies the same conditions at all boundaries and interfaces as the acoustic field (here expressed in terms of the velocity potential). Naturally, this is a superposition of modes,

$$G(x, x', (t - t')) = H(t - t')\Re \sum_{n=1}^{\infty} g_n(x, x')\, e^{-i\omega_n(t-t')}. \tag{16}$$

$H(t - t')$ denotes the Heaviside function; it guarantees causality. The quantities g_n (Green's function amplitude of mode n) and ω_n (modal frequencies if thermoacoustic coupling is absent) have been calculated analytically for the combustion system shown in Figure 6 (see Heckl[16] for details on the derivation); the results are:

$$g_n(x, x') = i\frac{\hat{g}(x, x', \omega_n)}{2\omega_n F(\omega_n)} \tag{17}$$

with

$$\hat{g}(x, x', \omega) = \begin{cases} D(x, \omega)C(x', \omega) & \text{for } L < x < x' \\ C(x, \omega)D(x', \omega) & \text{for } x' < x < \infty \end{cases} \tag{18}$$

and

$$C(x, \omega) = -ic\, e^{ik(x-L)}, \tag{19}$$

$$D(x, \omega) = F(\omega)\left(R_{CA}e^{ik(x-L)} + e^{-ik(x-L)}\right) + R_0 T_{AC}^2 e^{ikx}, \tag{20}$$

$$F(\omega) = e^{-i\omega Lc} - R_0 R_{AC} e^{i\omega Lc}. \tag{21}$$

$F(\omega)$ is the function appearing in the characteristic equation $F(\omega_n) = 0$, which determines the modal frequencies ω_n of the Green's function.

3.5 Stability analysis

In our case, the Green's function is a velocity potential. The governing equation for the velocity potential in the presence of unsteady heating is given by

$$\frac{1}{c^2}\frac{\partial^2 \phi}{\partial t^2} - \frac{\partial^2 \phi}{\partial x^2} = B\, q(x, t), \tag{22}$$

where $B = -(\gamma - 1)/c^2$ (abbreviation), and γ is the specific heat ratio. The term $q(x, t)$ is the fluctuating part of the heat release rate per unit mass of air, and for a compact flame (located at x_q), we can put

$$q(x, t) = q(t)\sigma(x - x_q). \tag{23}$$

Following the procedure in Heckl[16], we can convert equation (22) into an integral equation for the velocity $u'(t)$ at the heat source,

$$u'(t) = B\int_{t'=0}^{t} \left.\frac{\partial G(x, x', t - t')}{\partial x}\right|_{\substack{x = x_q \\ x' = x_q}} q(t')\, dt'. \tag{24}$$

We note that one has to distinguish between the velocity at the heat source position (x_q) and the velocity at the FDF reference position (x_{ref}). Here, however, we have the special case where $x_q \approx x_{ref}$ (Noiray's velocity measurements were taken at the base of the matrix flame), so we can denote both velocities with the same symbol $u'(t)$.

There is a direct physical interpretation of this equation: the acoustic velocity at observer time t and observer location x_q is given by the sum of velocity responses to a sequence of impulses produced at previous times t' at the same location.

If the modes are assumed to be non-interacting, equation (24) can be converted into an ODE for the velocity of an individual mode; the mathematical manipulations can be found in Heckl,[16] and the result is

$$\ddot{u}' - 2;\Im(\omega_n)\dot{u}' + |\omega_n|^2 u' = -B\Im(\omega_n G_n^*)q(t) + B\Re(G_n)\dot{q}(t), \tag{25}$$

where G_n is given by

$$G_n = \left.\frac{\partial g_n(x,x')}{\partial x}\right|_{\substack{x=x_q \\ x'=x_q}} = -\frac{c}{2L}R_0 T_{AC}^2 e^{2i\omega_n x_q/c}. \quad (26)$$

Clearly, equation (25) is the equation for a damped harmonic oscillator, forced by the fluctuating heat release rate $q(t)$ and its time derivative $\dot{q}(t)$. The problem is closed if we have an analytical expression for $q(t)$ in terms of $u'(t)$. This is provided by equation (6), which is an expression for the global heat release rate $Q'(t)$ and can be converted into local form,

$$q(t) = \alpha\left[n_1\int_{-\infty}^{\infty} u'(t-\tau)D(\tau-\tau_1)\mathrm{d}\tau + n_2\int_{-\infty}^{\infty} u'(t-\tau)D(\tau-\tau_2)\mathrm{d}\tau\right]; \quad (27)$$

α is a constant factor, given by

$$\alpha = \frac{\bar{Q}}{\bar{\rho}\bar{u}S}, \quad (28)$$

and S is the cross-sectional area of the tube.

In order to simplify the subsequent calculations we assume that $u'(t)$ is harmonic with an unknown frequency Ω, given by

$$u'(t) = A\cos\Omega t. \quad (29)$$

The time-lag terms $u'(t-\tau)$ in equation (27) can be rewritten and subsequent substitution into equation (25) gives simply (for details, see Appendix 3)

$$\ddot{u}' + a_1\dot{u}' + a_0 u' = 0, \quad (30)$$

with,

$$\begin{aligned} a_1 = &-2\Im(\omega_n) - B\Im(\omega_n G_n^*)\alpha\left[n_1\int_0^{\infty} D(\tau-\tau_1)\frac{\sin(\Omega\tau)}{\Omega}\mathrm{d}\tau + n_2\int_0^{\infty} D(\tau-\tau_2)\frac{\sin(\Omega\tau)}{\Omega}\mathrm{d}\tau\right] \\ &- B\Re(G_n)\alpha\left[n_1\int_0^{\infty} D(\tau-\tau_1)\cos(\Omega\tau)\mathrm{d}\tau + n_2\int_0^{\infty} D(\tau-\tau_2)\cos(\Omega\tau)\mathrm{d}\tau\right], \end{aligned} \quad (31)$$

and

$$\begin{aligned} a_0 = &\left|\omega_n^2\right| + B\Im(\omega_n G_n^*)\alpha\left[n_1\int_0^{\infty} D(\tau-\tau_1)\cos(\Omega\tau)\mathrm{d}\tau + n_2\int_0^{\infty} D(\tau-\tau_2)\cos(\Omega\tau)\mathrm{d}\tau\right] \\ &- B\Re(G_n)\alpha\left[n_1\int_0^{\infty} D(\tau-\tau_1)\Omega\sin(\Omega\tau)\mathrm{d}\tau + n_2\int_0^{\infty} D(\tau-\tau_2)\Omega\sin(\Omega\tau)\mathrm{d}\tau\right]. \end{aligned} \quad (32)$$

Equation (30) is the equation for a damped harmonic oscillator. a_1 is the damping coefficient and hence an indicator of the stability behaviour: mode n is stable if $a_1 \geq 0$ and unstable otherwise. a_0 is the square of the oscillator's eigenfrequency.

3.6 Stability predictions

We make stability predictions for the matrix burner with the properties listed in Table 2. Two parameters were varied to construct stability maps: the tube length L in the range from 0.1 m to 0.8 m, and the amplitude $A/\bar{u}$ in the range 0–2. We extrapolated the fitting parameters to unphysically high values of $A/\bar{u}$ to see whether we can detect a tendency for higher amplitudes (rather than to get reliable stability predictions for high amplitudes). The stability map for mode $n=1$ is shown in Figure 7(a). This was determined in the following way: for each point $(L, A/\bar{u})$ in the map, we calculated the coefficient a_1 from equation (30) (with ω_n from equation (21), and G_n from equation (26), both for mode $n=1$), and noted the sign of a_1. Points with $a_1 \geq 0$ (unstable) were marked in grey; points with $a_1 < 0$ (stable) were marked in white.

The unstable region has the shape of a band emerging from the bottom left corner and agrees qualitatively with Noiray's results[8,9] in the region where the experimental measurements are available. For comparison, the border of the instability region found by Noiray et al.[9] is also shown in Figure 7(a) by the dashed black curve. The quantitative agreement is less

Table 2. Geometry and other parameters of the matrix burner.

Parameter	Value
Tube radius, a	0.035 m
Length of the tube, L	0.1–0.8 m (variable)
Thickness of the perforated plate, h	0.003 m
Number of perforations per unit area, $\mathcal{N}$	$1.09 \times 10^5/\mathrm{m}^2$
Radius of perforations, r_p	0.001 m
factor relating local and global heat release rate, α	$3 \times 10^5 \mathrm{m}^2/\mathrm{s}^2$
Distance of flame from perforated plate, $x_q - L$	0.01 m
Specific heat ratio, γ	1.4
Speed of sound, c	345 m/s

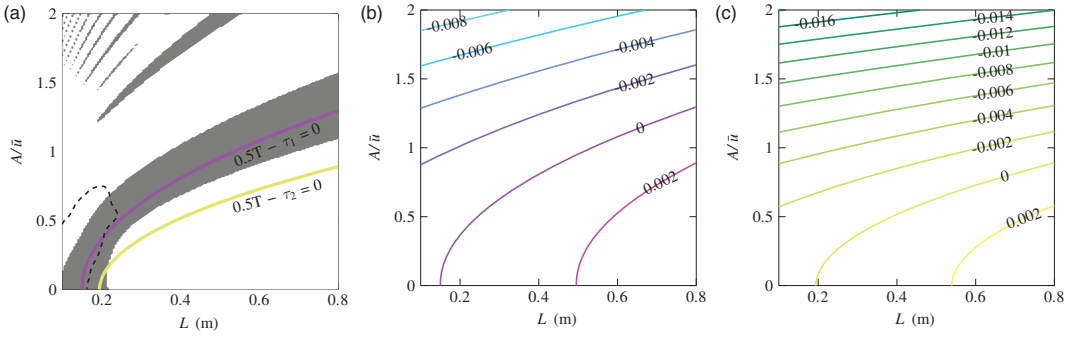

Figure 7. Stability map of a matrix burner using a two time-lag heat release rate law and Green's function approach. (a) Stability map (unstable regions are grey; the dashed curve shows the results from Noiray et al.[9]), (b) Contours of $(0.5T - \tau_1)$ and (c) contours of $(0.5T - \tau_2)$.

satisfactory. Our predictions overestimate the size of the instability region. The stability map given in Noiray[8] and Noiray et al.[9] was also obtained by extrapolating the FDF, however, this was done by setting the FDF gain to zero outside the measured frequency range. It is likely that the different extrapolation methods are responsible for the quantitative discrepancy between our stability map and that in Noiray[8] and Noiray et al.[9]

We now investigate the influence of the time-lags and their amplitude-dependence on the stability behaviour. In a quarter-wave resonator with a *single* time-lag τ in the heat release law, the stability behaviour switches from stable to unstable (or vice versa) as τ crosses the threshold $0.5T$, where $T = 4L/c$ is the period of mode 1 (the mode under consideration). With an amplitude-dependent τ, the switch happens when the amplitude reaches the value where $\tau = 0.5T$. If there are *two* prominent time-lags, τ_1 and τ_2, in the heat release law, we expect that they both influence the stability through their amplitude-dependence. In order to illustrate this, we have produced Figures 7(b) and (c). Figure 7(b) shows contours for the difference $(0.5T - \tau_1)$ and Figure 7(c) for the difference $(0.5T - \tau_2)$. The zero-contours, i.e. the contours $0.5T - \tau_1 = 0$ and $0.5T - \tau_2 = 0$, have been superimposed on the stability map in Figure 7(a). We observe that they are very similar in shape to the boundaries of the unstable region.

4. Conclusions and outlook

In this paper, we presented a systematic method to approximate a known FDF (obtained elsewhere by measurement or numerical simulations) by analytical expressions. After calculation of the corresponding UIR, it is possible to identify the time-lags that are prominent in the flame dynamics. We presume that these correspond to the travelling times of different perturbations (e.g. fluctuations in turbulence intensity or fluctuations in fuel concentration), and that therefore there are only a few prominent time-lags. The existence of just a few such prominent time-lags, each surrounded by a decaying distribution, allows us to represent the UIR as a superposition of Gaussian time-lag distributions. This representation is Fourier-transformed into the frequency domain and an analytical expression for the FTF or FDF is obtained; the frequency-dependence of the FTF/FDF is also a superposition of Gaussians.

We formulate a heat release rate law in the time-domain and frequency-domain with several fitting parameters: the prominent time-lags (τ_1, τ_2, ...), the standard deviations (σ_1, σ_2, ...) characterising the spread around each time-lag, and generalised coupling coefficients (n_1, n_2, ...). Thus our model has $3k$ parameters for k prominent time-lags.

Each of the fitting parameters is determined by minimising the discrepancy with the original FTF data. Our model is well-suited to capture the main features of a typical FTF: a value of 1 at zero frequency, an excess gain at low frequencies, a decay to zero at high frequencies (low-pass filter), and a phase curve with nearly constant slope at low frequencies. We also formulate the amplitude-dependence of the fitting parameters τ_1, τ_2, ..., σ_1, σ_2, ..., n_1, n_2, ... analytically. Altogether, a full analytical description of a measured FDF is obtained. These analytical expressions and the tailored Green's function can be used to predict the stability behaviour of the combustion system under consideration.

We applied this method to a specific laboratory burner (Noiray's matrix burner) and determined the analytical representation of its FDF. This was found to be very accurate (the percentage error in the gain is well below 10% for most frequencies and amplitudes). We subsequently used this analytical FDF to make stability predictions (based on a Green's function approach) and presented them in the form of a stability

map. We obtained good qualitative agreement with Noiray's measured stability map. Also, we observed that the stability map is quite sensitive to the fitting parameters and the analytical description of their amplitude-dependence. Additional physical insight can be used to obtain good accuracy.

The multiple time-lag model is an improvement of the extended $n\tau$ model, which is somewhat hypothetical in that it features a single time-lag term $u'(t-\tau)$ and an instantaneous time-lag term $u'(t)$; it has been used by Heckl[16,19] and Bigongiari and Heckl.[20] The multiple time-lag model has the following advantages:

- It determines the time-lags from the UIR of the flame and is thus not only physically more sound, but also closer to the actual data.
- It captures all key features of a typical measured FDF: a gain of unity at zero frequency, excess gain at low frequencies, and low-pass filter behaviour.
- It gives good stability predictions, which are qualitatively similar to those obtained by Noiray.

Our paper gives a good analytical approximation for the nonlinear heat release rate (FDF). It also provides a fast prediction tool for the stability of a combustion system using this heat release rate law and tailored Green's function. Our multiple time-lag model can be applied for any flame with known FDF. Our stability analysis, which is based on the Green's function, can be applied to any combustor configuration, for which the tailored Green's function is known analytically. In this paper, we have calculated the tailored Green's function for a rather simple configuration: a quarter-wave resonator with a temperature jump. This calculation can be extended to more complex configurations, provided that these can be modelled as a combination of 1D elements. Features that can be included in our model are for example: dump plane between tube sections, orifice between tube sections, frequency-dependent reflection coefficients at the inlet and outlet.

However, not included in this paper are losses in the combustion system and thus we over-predict the unstable region. This will be addressed in a future paper.

Acknowledgements

The presented work is part of the Marie Curie Initial Training Network Thermoacoustic and Aeroacoustic Nonlinearities in Green combustors with Orifice structures (TANGO).

Declaration of Conflicting Interests

The author(s) declared no potential conflicts of interest with respect to the research, authorship, and/or publication of this article.

Funding

The author(s) disclosed receipt of the following financial support for the research, authorship, and/or publication of this article: We gratefully acknowledge the financial support from the European Commission under call FP7-PEOPLE-ITN-2012.

References

1. Lieuwen TC and Yang V. Combustion instabilities in gas turbine engines: operational experience, fundamental mechanisms, and modeling. In: *Progress in astronautics and aeronautics*. Vol. 210, Virginia, USA: American Institute of Aeronautics and Astronautics, Inc., 2005.
2. Crocco L. Aspects of combustion stability in liquid propellant rocket motors. Part I: Fundamentals. Low frequency instability with monopropellants. *J Am Rocket Soc* 1951; 21: 163–178.
3. Schuermans B. *Modeling and control of thermoacoustic instabilities*. PhD Thesis, École Polytechnique Fédérale De Lausanne, 2003.
4. Schuermans B, Bellucci V, Guethe F, et al. A detailed analysis of thermoacoustic interaction mechanism in a turbulent premixed flame. In: *Proceedings of ASME Turbo Expo*, Power for Land, Sea and Air, Vienna, Austria, 14–17 June 2004.
5. Komarek T and Polifke W. Impact of swirl fluctuations on the flame response of a perfectly premixed swirl burner. *J Eng Gas Turbines Power* 2010; 132: 061503-1–061503-7.
6. Bade S, Wagner M, Hirsch C, et al. Design for thermo-acoustic stability: modeling of burner and flame dynamics. *J Eng Gas Turbines Power* 2013; 135: 111502-111502–7.
7. Subramanian P, Blumenthal RS, Polifke W, et al. Distributed time lag response functions for the modeling of combustion dynamics. *Combust Theory Model* 2015; 19: 223–237.
8. Noiray N. *Linear and nonlinear analysis of combustion instabilities, application to multipoint injection systems and control strategies*. PhD Thesis, École Centrale Paris, 2007.
9. Noiray N, Durox D, Schuller T, et al. A unified framework for nonlinear combustion instability analysis based on the flame describing function. *J Fluid Mech* 2008; 615: 139–167.
10. Ćosić B, Moeck JP and Paschereit CO. Nonlinear instability analysis for partially premixed swirl flames. *Combust Sci Technol* 2014; 186: 713–736.
11. Polifke W, Kopitz J and Serbanovic A. Impact of the fuel time lag distribution in elliptical premix nozzles on combustion stability. In: *7th AIAA/CEAS aeroacoustics conference and exhibit*, Maastricht, The Netherlands, 28–30 May 2001.
12. Flohr P, Paschereit CO, van Roon B, et al. Using CFD for time-delay modeling of premix flames. In: *Proceedings of ASME Turbo Expo 2001*, New Orleans, Louisiana, USA, 4–7 June 2001.
13. Flohr P, Paschereit CO and Bellucci V. Steady CFD analysis for gas turbine burner transfer functions. In: *41st*

AIAA aerospace sciences meeting and exhibit, Reno, Nevada, USA, 6–9 January 2003.
14. Tay-Wo-Chong L, Bomberg S, Ulhaq A, et al. Comparative validation study on identification of premixed flame transfer function. *J Eng Gas Turbines Power* 2011; 134: 021502-021502–8.
15. Iurashev D, Campa G and Anisimov V. Response of swirl stabilized perfectly premixed flame to high-amplitude velocity excitations. In: *The 23rd International Congress on Sound and Vibration*, Athens, Greece, July 2016.
16. Heckl MA. Analytical model of nonlinear thermoacoustic effects in a matrix burner. *J Sound Vib* 2013; 332: 4021–4036.
17. Palies P, Durox D, Schuller T, et al. Nonlinear combustion instability analysis based on the flame describing function applied to turbulent premixed swirling flames. *Combust Flame* 2011; 158: 1980–1991.
18. Li J and Morgans AS. Time domain simulations of nonlinear thermoacoustic behaviour in a simple combustor using a wave-based approach. *J Sound Vib* 2015; 346: 345–360.
19. Heckl M. A new perspective on the flame describing function of a matrix flame. *Int J Spray Combust Dyn* 2015; 7: 91–112.
20. Bigongiari A and Heckl MA. A Green's function approach to the rapid prediction of thermoacoustic instabilities in combustors. *J Fluid Mech* 2016; 798: 970–996.
21. Gopinathan SM, Bigongiari A and Heckl MA. Time-domain representation of a flame transfer function with generalised $n\tau$ – law featuring a time-lag distribution. In: *Proceedings of the 23rd international congress on sound and vibration*, Athens, Greece, 10–14 July 2016.
22. Polifke W. Black-box system identification for reduced order model construction. *Ann Nuclear Energy* 2014; 67: 109–128.
23. Heckl MA and Howe MS. Stability analysis of the rijke tube with a green's function approach. *J Sound Vib* 2007; 305: 672–688.
24. Gradshteyn IS and Ryzhik IM. *Table of integrals, series and products*, 4th ed. London: Academic Press, 1980.
25. Howe MS. *Acoustics of fluid–structure interaction*. Cambridge: Cambridge University Press, 1998.
26. Levine H and Schwinger J. On the radiation of sound from an unflanged circular pipe. *Phys Rev* 1948; 73: 383–406.

Appendix 1. Derivation of the FTF for the heat release rate law with multiple time-lags and Gaussian distribution of time-lags

We assume that the distributions in equation (6) are such that $D(\tau-\tau_j)\approx 0$, for $\tau<0$ $(j=1,2,\ldots,k)$; then we can extend the integration range from $(0,\infty)$ to $(-\infty,+\infty)$ and apply the Fourier Transform to equation (6),

$$\mathcal{F}\left(\frac{Q'(t)}{\bar{Q}}\right)=\mathcal{F}\left(\overbrace{n_1\int_{-\infty}^{\infty}\frac{u'(t-\tau)}{\bar{u}}D(\tau-\tau_1)\mathrm{d}\tau}^{\text{Term 1}}+\overbrace{n_2\int_{-\infty}^{\infty}\frac{u'(t-\tau)}{\bar{u}}D(\tau-\tau_2)\mathrm{d}\tau}^{\text{Term 2}}+\cdots+\overbrace{n_k\int_{-\infty}^{\infty}\frac{u'(t-\tau)}{\bar{u}}D(\tau-\tau_k)\mathrm{d}\tau}^{\text{Term k}}\right). \tag{33}$$

The Fourier transform of the LHS of equation (33) is

$$\mathcal{F}\left(\frac{Q'(t)}{\bar{Q}}\right)=\frac{\hat{Q}(\omega)}{\bar{Q}}. \tag{34}$$

By applying the convolution theorem, 'Term j' in equation (33) can be written as

$$\mathcal{F}\left(n_j\int_{-\infty}^{\infty}\frac{u'(t-\tau)}{\bar{u}}D(\tau-\tau_j)\mathrm{d}\tau\right)=n_j\mathcal{F}\left(\frac{u'(t)}{\bar{u}}\right)\mathcal{F}\big(D(\tau-\tau_j)\big). \tag{35}$$

Also,

$$\mathcal{F}\left(\frac{u'(t)}{\bar{u}}\right)=\frac{\hat{u}(\omega)}{\bar{u}}\quad\text{and}\quad\mathcal{F}\big(D(\tau-\tau_j)\big)=\mathcal{F}(D(\tau))e^{i\omega\tau_j}, \tag{36}$$

and the Fourier transform of the Gaussian function $D(\tau)$ is[24]

$$\mathcal{F}(D(\tau))=e^{\frac{-\omega^2\sigma^2}{2}}. \tag{37}$$

'Term j' now becomes

$$\mathcal{F}\left(n_j\int_{-\infty}^{\infty}\frac{u'(t-\tau)}{\bar{u}}D(\tau-\tau_j)\mathrm{d}\tau\right)=n_j\frac{\hat{u}(\omega)}{\bar{u}}e^{i\omega\tau_j}e^{\frac{-\omega^2\sigma_j^2}{2}}. \tag{38}$$

Combination of equations (34), (38) and (33) gives

$$\frac{\hat{Q}(\omega)}{\bar{Q}}=n_1\frac{\hat{u}(\omega)}{\bar{u}}e^{i\omega\tau_1}e^{\frac{-\omega^2\sigma_1^2}{2}}+n_2\frac{\hat{u}(\omega)}{\bar{u}}e^{i\omega\tau_2}e^{\frac{-\omega^2\sigma_2^2}{2}}+\cdots+n_k\frac{\hat{u}(\omega)}{\bar{u}}e^{i\omega\tau_k}e^{\frac{-\omega^2\sigma_k^2}{2}} \tag{39}$$

and

$$\mathcal{T}_k(\omega) = \frac{\frac{\hat{Q}(\omega)}{\bar{Q}}}{\frac{\hat{u}(\omega)}{\bar{u}}} = n_1 e^{i\omega\tau_1} e^{\frac{-\omega^2\sigma_1^2}{2}} + n_2 e^{i\omega\tau_2} e^{\frac{-\omega^2\sigma_2^2}{2}} + \cdots + n_k e^{i\omega\tau_k} e^{\frac{-\omega^2\sigma_k^2}{2}}. \quad (40)$$

Appendix 2. Reflection and transmission coefficients at the interfaces

The pressure reflection and transmission coefficient for the combined interface have been derived in Heckl.;[16] the results are:

$$R_{AC} = \frac{R_{AB} - R_{AB}R_{BA}R_{BC} + T_{AB}T_{BA}T_{BC}}{1 - R_{BA}R_{BC}} \text{ and } T_{AC} = \frac{T_{AB}T_{BC}}{1 - R_{BA}R_{BC}}. \quad (41)$$

R_{AB}, T_{AB} are the coefficients of the perforated plate; these are given by (see Howe,[25] p. 361)

$$R_{AB} = \frac{\omega}{\omega + 2i\mathcal{N}cK} \text{ and } T_{AB} = \frac{2i\mathcal{N}cK}{\omega + 2i\mathcal{N}cK}, \quad (42)$$

where $\mathcal{N}$ is the number of holes per unit area, and K is the Rayleigh conductivity. For a plate of thickness h and with circular holes of radius r_p (see Howe[25,p. 356]),

$$K = \frac{r_p^2\pi}{r_p\pi/2 + h}. \quad (43)$$

R_{BC} is the reflection coefficient of an unflanged open tube end; for a tube with radius a, it is given by Levine and Schwinger[26]

$$R_{BC} = -\frac{1 - [(1/4)(\omega a/c^2) - i(\omega a/c)0.6133]}{1 + [(1/4)(\omega a/c^2) - i(\omega a/c)0.6133]}. \quad (44)$$

The wave radiated from the open end is modelled by a complex 'transmission coefficient', T_{BC}, which is constructed in the following way: its magnitude is chosen such that acoustic energy is conserved, i.e. $|R_{BC}|^2 + |T_{BC}|^2 = 1$, and its phase is chosen such that the velocity has continuous phase at the tube end. This gives

$$T_{BC} = |T_{BC}|e^{i\varphi}, \text{ with } |T_{BC}| = \sqrt{1 - |R_{BC}|^2} \text{ and } \varphi = Arg(1 - R_{BC}). \quad (45)$$

Appendix 3. Harmonic oscillator equation for a single mode

The local heat release rate fluctuation $q'(x,t)$ is related to its global counterpart $Q'(t)$by $Q'(t) = \int q'(x,t)\bar{\rho}\mathrm{d}V$, where the integration is taken over the volume of the flame. This reduces to $q(t) = Q'(t)/(\bar{\rho}S)$ for a compact flame described by equation (23). Hence, with equations (6) and (28), we can write $q(t)$ as

$$q(t) = \frac{Q'(t)}{\bar{\rho}S} = \alpha\left[n_1\int_{-\infty}^{\infty} u'(t-\tau)D(\tau-\tau_1)\mathrm{d}\tau + n_2\int_{-\infty}^{\infty} u'(t-\tau)D(\tau-\tau_2)\mathrm{d}\tau\right], \quad (46)$$

and its derivative as

$$\dot{q}(t) = \alpha\left[n_1\int_{-\infty}^{\infty} \dot{u}'(t-\tau)D(\tau-\tau_1)\mathrm{d}\tau + n_2\int_{-\infty}^{\infty} \dot{u}'(t-\tau)D(\tau-\tau_2)\mathrm{d}\tau\right]. \quad (47)$$

In order to simplify equation (46), we assume that $u'(t)$ is harmonic with an unknown frequency Ω, given by

$$u'(t) = A\cos\ \Omega t, \quad (48)$$

and

$$\dot{u}'(t) = -A\Omega\ \sin\ \Omega t. \quad (49)$$

The time-lagged terms $u'(t-\tau)$ and $\dot{u}'(t-\tau)$ can be written with the trigonometric addition formulae as

$$u'(t-\tau) = u'(t)\cos\Omega\tau - \frac{\dot{u}'(t)}{\Omega}\sin\Omega\tau \quad (50)$$

and

$$\dot{u'}(t-\tau) = u'(t)\Omega\sin\Omega\tau + \dot{u}'(t)\cos\Omega\tau. \quad (51)$$

The local heat release rate fluctuation $q(t)$ and its derivative then become

$$q(t) = \alpha\left[n_1\int_0^\infty D(\tau-\tau_1)(u'(t)\Omega\sin\Omega\tau + \dot{u}'(t)\cos\Omega\tau)\mathrm{d}\tau + n_2\int_0^\infty D(\tau-\tau_2)(u'(t)\Omega\sin\Omega\tau + \dot{u}'(t)\cos\Omega\tau)\tau\mathrm{d}\tau\right], \quad (52)$$

and

$$\dot{q}(t) = \alpha\left[n_1\int_0^\infty D(\tau-\tau_1)\left(u'(t)\cos\Omega\tau - \frac{\dot{u}'(t)}{\Omega}\sin\Omega\tau\right)\mathrm{d}\tau + n_2\int_0^\infty D(\tau-\tau_2)\left(u'(t)\cos\Omega\tau - \frac{\dot{u}'(t)}{\Omega}\sin\Omega\right)\tau\mathrm{d}\tau\right]. \quad (53)$$

The frequency Ω can be approximated by $\Omega \approx Re(\omega_n)$. Substituting equations (52) and (53) into equation (25), and sorting the many terms, we get equation (30).